Tellus
SERIES B CHEMICAL AND PHYSICAL METEOROLOGY
PUBLISHED BY THE INTERNATIONAL METEOROLOGICAL INSTITUTE IN STOCKHOLM

Tellus (2011), 63B, 165–180

TELLUS

Amount and timing of permafrost carbon release in response to climate warming

By KEVIN SCHAEFER[1]*, TINGJUN ZHANG[1], LORI BRUHWILER[2] and ANDREW P. BARRETT[1], [1]*National Snow and Ice Data Center, Cooperative Institute for Research in Environmental Sciences, University of Colorado at Boulder, Boulder, CO 80309, USA;* [2]*National Oceanic and Atmospheric Administration, Earth System Research Laboratory, Boulder, CO, USA*

(Manuscript received 31 December 2009; in final form 5 January 2011)

ABSTRACT

The thaw and release of carbon currently frozen in permafrost will increase atmospheric CO_2 concentrations and amplify surface warming to initiate a positive permafrost carbon feedback (PCF) on climate. We use surface weather from three global climate models based on the moderate warming, A1B Intergovernmental Panel on Climate Change emissions scenario and the SiBCASA land surface model to estimate the strength and timing of the PCF and associated uncertainty. By 2200, we predict a 29–59% decrease in permafrost area and a 53–97 cm increase in active layer thickness. By 2200, the PCF strength in terms of cumulative permafrost carbon flux to the atmosphere is 190 ± 64 Gt C. This estimate may be low because it does not account for amplified surface warming due to the PCF itself and excludes some discontinuous permafrost regions where SiBCASA did not simulate permafrost. We predict that the PCF will change the arctic from a carbon sink to a source after the mid-2020s and is strong enough to cancel 42–88% of the total global land sink. The thaw and decay of permafrost carbon is irreversible and accounting for the PCF will require larger reductions in fossil fuel emissions to reach a target atmospheric CO_2 concentration.

1. Introduction

Permafrost regions in the Northern Hemisphere contain an estimated 1672 Gt of carbon (Tarnocai et al., 2009). Of this, 818 Gt of carbon is in the top 3 m of soil located in regions with permanently frozen soil or permafrost, 648 Gt is frozen in deposits known to extend below 3 m and 206 Gt is in the top 3 m of soil located in regions without permafrost (Tarnocai et al., 2009). Permafrost is soil at or below 0 °C for at least two consecutive years. Measurements of ^{14}C in Siberia indicate this carbon was frozen during or since the last ice age (Dutta et al., 2006). Estimates of total permafrost carbon are based primarily on observations in Siberia and Alaska. Recent measurements indicate Canadian permafrost also has a significant store of frozen organic matter (Tarnocai, 1997; Ping et al., 2008). Although uncertain, the total amount of frozen permafrost carbon is on par with the amount of carbon currently in the atmosphere.

This frozen permafrost carbon was buried by slow sedimentation processes that increased overall soil depth during or since the last ice age. Aeolian dust deposition, alluvial sedimentation or vertical peat deposition slowly increased soil depth on time scales of decades to millennia (Schuur et al., 2008). Active layer thickness (ALT) stayed relatively constant so the permafrost horizon also rose with soil depth, freezing roots and organic material at the bottom of the active layer into permafrost (Zimov et al., 2006a,b). The active layer is the surface layer of soil that thaws each summer and freezes each winter. Cryoturbation caused by annual freeze/thaw cycles in the active layer accelerated the burial process by mixing carbon-rich organic soil from the surface down to the permafrost horizon (Schuur et al., 2008). Thinning active layers during glacial periods also froze carbon into permafrost, but this carbon decayed as the ALT increased during inter-glacial periods (Zech et al., 2008). Microbial activity essentially stops once the soil is frozen, effectively removing this organic matter from the active carbon cycle.

Recent observations indicate widespread permafrost degradation in the Northern Hemisphere (Lemke et al., 2007). Permafrost temperatures at 20 m depth increased 2–3 °C increase in the last two decades (Osterkamp, 2007). Permafrost temperatures at depths up to 20 m increased 0–2 °C in Canada (Smith et al., 2004; Lemke et al., 2007), 0.3–2.8 °C at depths up to 10 m in Siberian Arctic and sub-Arctic (Lemke et al., 2007), 0.2–0.5 °C at 10 m depth on the Tibetan Plateau (Cheng and Wu, 2007; Lemke et al., 2007; Wu and Zhang, 2008). ALT has increased in Siberia since the 1950s (Brown et al., 2000; Frauenfeld et al., 2004; Zhang et al., 2005; Lemke et al., 2007). On the Tibetan plateau, ALT has increased (Wu and Zhang, 2010), the lower limit of the permafrost boundary has climbed to higher

*Corresponding author:
e-mail: kevin.schaefer@nsidc.org
DOI: 10.1111/j.1600-0889.2011.00527.x

elevations, and talik area has increased (Nan et al., 2003). A talik is a layer of unfrozen soil above permafrost, but below the seasonally frozen, surface soil layer. Thermokarst development has increased in permafrost regions (Jorgenson and Osterkamp, 2005). A thermokarst is a local subsidence or soil collapse due to the melting of ice and subsequent drainage of soil water from permafrost. A thermokarst or thaw lake is a shallow body of freshwater formed in a depression by melt water from thawing permafrost. Total thaw lake area and number in Siberia have increased in continuous permafrost and decreased in discontinuous permafrost (Smith et al., 2005).

Model projections predict increased permafrost degradation in the 21st century driven by surface warming, but these projections vary widely in the extent and degree of degradation. Zhang et al. (2008a,b) predict a 16–20% decrease in permafrost area in Canada between 2000 and 2100; Saito et al. (2007) predict a 40–57% reduction in the permafrost area in the Northern Hemisphere; Lawrence and Slater (2005) predict a 60–90% reduction and Lawrence et al. (2008) predict an 80–85% reduction. Projections of the increase in ALT are equally broad, ranging from 41% to 100% (Anisimov, 2007; Saito et al., 2007; Sushama et al., 2007; Zhang et al., 2008a,b). Although these projections vary widely on the exact amount of permafrost degradation, there is agreement that the areal extent of permafrost will decrease and the active layer will deepen.

Ubiquitous wetlands and lakes in permafrost regions indicate that some portion of carbon emitted to the atmosphere will be released as methane. Wetlands cover ~17% of permafrost globally and 50–80% of regions in west Siberia (Matthews and Fung, 1987). Methane emissions between 65°N and 70°N have risen in recent decades with maxima in winter and spring, indicating decay in thaw bulbs under thaw lakes (Walter et al., 2006). Thermokarst erosion as thaw lakes expand introduces organic matter from permafrost into the anaerobic lake bottom, accounting for 90% of methane emissions from Siberian thaw lakes. Measurements of ^{14}C show ages of 35,260 to 42,900 years, consistent with the decay of permafrost carbon (Walter et al., 2006). Atmospheric methane concentrations are much less than CO_2 and methane has a photochemical lifetime only on the order of a decade. However, methane is a much more effective greenhouse gas than CO_2, producing the second largest surface radiative forcing due to anthropogenic greenhouse gases after CO_2 (IPCC, 2007).

The permafrost carbon feedback (PCF) is an amplification of surface warming due to the release into the atmosphere of carbon currently frozen in permafrost (Fig. 1). As atmospheric CO_2 and methane concentrations increase, surface air temperatures will increase, causing permafrost degradation and thawing some portion of the permafrost carbon. Once permafrost carbon thaws, microbial decay will resume, increasing respiration fluxes to the atmosphere and atmospheric concentrations of CO_2 and methane. This will in turn amplify the rate of atmospheric warming and accelerate permafrost degradation, resulting in a positive PCF feedback loop on climate (Zimov et al., 2006b).

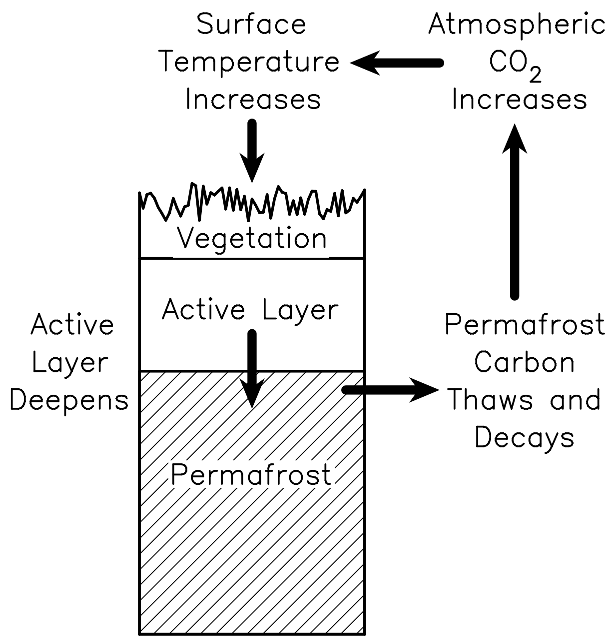

Fig. 1. A schematic showing the basic dynamics of the permafrost carbon feedback (PCF).

Little is known about the magnitude and dynamics of the PCF. The thaw and decay of even a small portion of the permafrost carbon could have substantial effects on atmospheric CO_2 and methane concentrations. However, none of the climate projections in the Intergovernmental Panel on Climate Change (IPCC) Fourth Assessment Report, none of the recent permafrost projections, and none of the projections of the terrestrial carbon cycle account for the PCF (Kicklighter et al., 1999; Cramer et al., 2001; Lawrence and Slater, 2005; Friedlingstein et al., 2006; Lemke et al., 2007; Zhang et al., 2008a,b; Qian et al., 2010). An estimate based on observed carbon fluxes predicts a global permafrost carbon flux of 0.8–1.1 Gt C yr^{-1} by 2100, but this estimate is very uncertain because it is based on a single site at Eight Mile Lake in Alaska (Schuur et al., 2009). A regional model projection with permafrost carbon predicts a complete thaw of permafrost in eastern Siberia by 2300, fuelled by the heat of microbial decay (Khvorostyanov et al., 2008). However, this regional projection did not include plant photosynthetic uptake, and so could not assess the strength and timing of the PCF.

Here we make initial estimates of the strength and timing of the PCF using model projections of permafrost degradation and carbon flux. We quantify how much permafrost carbon will thaw and when, identify permafrost regions most vulnerable to thaw and quantify sources of uncertainty. Schuur et al. (2008) identified four mechanisms that result in the release of permafrost carbon to the atmosphere: active layer thickening, talik formation, erosion and thermokarst development. We will address the effects of active layer thickening and talik formation, but not river and coastal erosion and thermokarst development. Our projections do not include methane production from wetlands. The model is run in an 'off-line' mode, where weather data forces the land surface model, ignoring land–atmosphere feedbacks. This off-line configuration does not account for amplified surface radiative forcing (the atmospheric portion of the PCF), but does allows us to estimate the PCF strength in terms of permafrost carbon flux to the atmosphere.

2. Methods

We used the Simple Biosphere/Carnegie-Ames-Stanford Approach (SiBCASA) model (Schaefer et al., 2008) to run projections of the terrestrial carbon cycle from 1973 to 2200 for continuous and discontinuous permafrost north of 45° latitude. We spun SiBCASA up to steady-state initial conditions using input weather from the European Center for Medium range Weather Forecasting re-analysis (ERA40) from 1973 to 2001 (Uppala et al., 2005). From 2002 to 2200, we randomly selected ERA40 years and applied three different warming rates (high, medium and low) based on the A1B IPCC scenario (IPCC, 2007). We added a new permafrost carbon pool in the soil column below a threshold depth. When the active layer deepened below the threshold depth, SiBCASA reset the threshold depth, thawed the permafrost carbon and transferred it to the active soil carbon pools. For each assumed warming rate, we ran two projections, one with permafrost carbon and one without. The strength of the PCF in terms of total permafrost carbon flux to the atmosphere is the difference between these two simulations. We scaled the permafrost carbon flux to estimate uncertainty associated with assumed permafrost carbon content and subgrid permafrost extent. The ensemble mean of all projections represents our best estimate of the PCF strength and the ensemble standard deviation represents uncertainty.

2.1. SiBCASA description

SiBCASA combines the biophysical Simple Biosphere model, version 3.0 (SiB3.0), with the carbon biogeochemistry from the Carnegie-Ames-Stanford Approach (CASA) model (Schaefer et al., 2008). SiBCASA has fully integrated water, energy and carbon cycles and computes surface energy and carbon fluxes at 10-min time steps. SiBCASA predicts the moisture content, temperature and carbon content of the canopy, canopy air space and soil (Sellers et al., 1996a; Vidale and Stockli, 2005). Fluxes of latent and sensible heat include the effects of snow cover, rainfall interception by the canopy, and aerodynamic turbulence (Sellers et al., 1996a).

To calculate plant photosynthesis, SiBCASA uses a modified Ball-Berry stomatal conductance model (Collatz et al., 1991; Ball, 1998) coupled to a C3 enzyme kinetic model (Farquhar et al., 1980) and a C4 photosynthesis model (Collatz et al., 1992). Leaf photosynthesis is scaled to the canopy level using the absorbed fraction of Photosynthetically Active Radiation (fPAR) derived from remotely sensed normalized difference vegetation index (NDVI) fields (Sellers et al., 1994, 1996b). Our projections used an average seasonal cycle in fPAR derived from the GIMMS NDVI data set (Tucker et al., 2005). SiBCASA uses biome specific biophysical parameters based on the ISLSCP biome classification map and soil textures of percent sand, silt and clay interpolated from the International Global Biosphere Program soil core database.

SiBCASA predicts soil organic matter, surface litter and live biomass (leaves, roots and wood) in a system of 13 prognostic carbon pools (Schaefer et al., 2008). SiBCASA biogeochemistry does not account for disturbances, such as fire, and does not include a nitrogen cycle. Each time biomass moves from one pool to another, some carbon is lost as respiration. SiBCASA separately calculates respiration losses due to microbial decay (heterotrophic respiration) and plant growth (autotrophic respiration). The decay of carbon in the soil varies with soil temperature and moisture as a function of depth. The temperature response accounts for rapidly declining microbial activity below freezing (Schaefer et al., 2008).

SiBCASA uses a coupled soil temperature and hydrology model with explicit treatment of frozen soil water originally from the Community Climate System Model, Version 2.0 (Bonan, 1996; Oleson et al., 2004). To improve simulated soil temperatures, Schaefer et al. (2009) expanded the soil model to 25 layers, with geometrically increasing thickness, from 2 to 280 cm, to a total depth of 15 m. Schaefer et al. (2009) also added the effects of soil organic matter on soil physical properties.

SiBCASA includes a prognostic snow model based on the Community Land Model in the Community Climate System Model, Version 3.0 (Dai et al., 2003; Oleson et al., 2004). The snow model has a variable number of snow layers up to a maximum of five, depending on snowfall amount and history. Snow density and depth, and thus thermal conductivity, varies with time, accounting for the effects of thermal aging, weight compaction and melting. To improve simulated soil temperature at high latitudes, particularly in permafrost, Schaefer et al. (2009) added the effects of depth hoar and wind compaction on simulated snow density and depth.

We added a permafrost carbon pool below a threshold soil depth, D_{min}, and above a maximum soil depth, D_{max} of 3 m (Fig. 2). D_{min} represents the maximum thaw depth since the end of the last ice age and we assume above D_{min}, the permafrost has thawed frequently enough over thousands of years such that old organic matter has decayed away (Zech et al., 2008). Permafrost can extend down hundreds of metres, but in most regions, the bulk of permafrost carbon is located in the top 3 m of soil, although some highly localized deposits of permafrost carbon can extend well below 3 m depth (Tarnocai et al., 2009). We focused on thawing of permafrost carbon in the top 3 m of soil and assume a constant, spatially uniform D_{max} of 3 m. Within the permafrost carbon layer, we assume a uniform permafrost carbon density of 21 kg C m^{-3}, ~2% carbon by mass (including

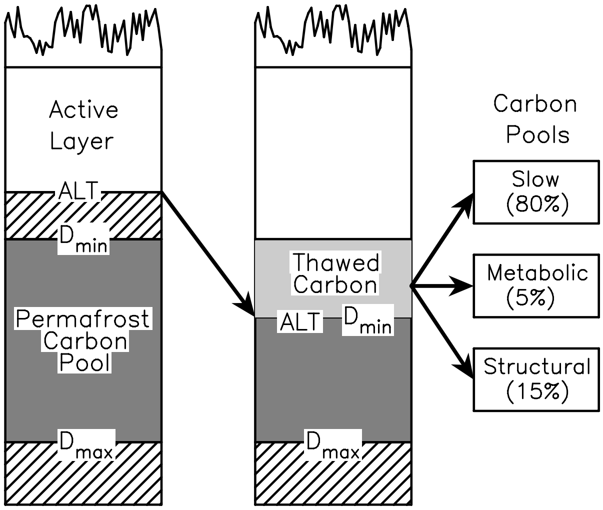

Fig. 2. The SiBCASA permafrost carbon pool. D_{min} represents the maximum depth of thaw since the end of the last ice age and D_{max} is the maximum depth of the permafrost carbon pool. When the active layer thickness (ALT) exceeds D_{min} as temperature rises, SiBCASA resets D_{min} to ALT and transfers the thawed permafrost carbon to the soil carbon pools.

ice content). This is well within the range of observed values: less than observed carbon densities of 33 kg C m^{-3} in yedoma soils in Siberia (Dutta et al., 2006; Khvorostyanov et al., 2008; Zech et al., 2008), but higher than observed densities of 13 kg C m^{-3} in Alaska (Ping et al., 2008).

D_{min} in each grid cell is initially set to the maximum simulated ALT plus 1% from 1973 to 2001. The 1% increase accounts for our criteria on simulated ALT for steady-state initial conditions (see 'Simulation setup'). If the maximum ALT for a particular grid cell exceeds D_{max}, we assume that pixel contains no permafrost carbon. This occurred in regions of discontinuous permafrost where SiBCASA was unable to simulate permafrost (see 'Results'). After 2001, when ALT exceeds D_{min} as temperatures increase, SiBCASA resets D_{min} to ALT, calculates the volume of thawed soil and transfers the thawed permafrost carbon to the active soil carbon pools. We divide the thawed carbon between active carbon pools in the appropriate soil layer based on observed fractions of labile material from permafrost samples in Siberia (Dutta et al., 2006). Once D_{min} exceeds D_{max} (which stays constant at 3 m), no additional permafrost carbon is thawed.

2.2. Simulation setup

As input weather, we use the ERA40 reanalysis from 1973 to 2001 (Uppala et al., 2005) and our domain is continuous and discontinuous permafrost regions north of 45°N latitude (Brown et al., 1998; Zhang et al., 1999). We exclude sporadic and isolated permafrost regions and areas dominated by glaciers in Greenland and many of the islands in northeast Canada. From 2002 to 2200 we randomly assign years of ERA40 weather from 1973 to 2001. Randomly selecting years eliminates repeating patterns of inter-annual variability in model output that would result from repeating a multiyear block of ERA40 weather. The ERA40 data set includes surface air temperature, water vapour mixing ratio, precipitation, radiation, pressure and wind speed every 6 h. Except for incident solar radiation, SiBCASA linearly interpolates in time between ERA40 data points to the SiBCASA time step of 10 min. We scale incident solar radiation by the cosine of the solar zenith angle to conserve incoming energy and assure no light falls on the canopy at night (Zhang et al., 1996).

Table 1. Warming rates for the 21st century (°C century^{-1}) per month from three models driven by IPCC scenario A1B (rates for the 22nd century appear in parentheses)

Month	High warming CCSM3 (°C century^{-1})	Medium warming HadCM3 (°C century^{-1})	Low warming MIROC3.2 (°C century^{-1})
Jan	9.66 (1.11)	6.86 (0.53)	7.43 (−0.06)
Feb	9.21 (0.93)	6.39 (0.47)	5.10 (0.01)
Mar	7.14 (0.20)	6.01 (0.08)	4.42 (−0.04)
Apr	5.67 (0.63)	4.55 (0.34)	3.21 (0.04)
May	4.77 (0.37)	3.73 (0.13)	2.51 (−0.11)
Jun	5.23 (0.69)	4.18 (0.38)	2.95 (0.06)
Jul	4.86 (0.24)	4.82 (−0.07)	3.24 (−0.38)
Aug	5.62 (0.38)	5.47 (0.20)	3.57 (0.01)
Sep	5.63 (0.37)	4.59 (0.10)	3.91 (−0.17)
Oct	7.03 (0.48)	5.11 (0.32)	5.46 (0.15)
Nov	8.80 (0.67)	6.85 (0.69)	7.41 (0.71)
Dec	9.78 (0.50)	6.98 (0.01)	7.40 (−0.49)

After 2001 we superimpose linear change rates onto the input weather from three models driven by the A1B IPCC scenario. The IPCC developed 40 Greenhouse Gas Emissions scenarios grouped in four distinct families, each representing a 'storyline' of possible future changes in population, economic development and energy use (Nakicenovic et al., 2000). In the A1B scenario, the atmospheric CO_2 increases from current values to 700 ppm by 2100, then stays constant at 700 ppm after 2100. We chose the A1B scenario because it represents a 'middle of the road' scenario that has been used in other climate change impact studies. We selected simulations from three models for the A1B scenario: the Model for Interdisciplinary Research on Climate (MIROC3.2), the Hadley Centre Climate Model Version 3 (HadCM3) and the Community Climate System Model Version 3 (CCSM3). We refer to these as high, medium and low projected warming rates respectively, but these do not necessarily represent high, medium and low warming rates for the entire suite of climate models run using IPCC scenarios.

We superimposed spatially uniform, linear increases in air temperature, precipitation and incident solar radiation onto the ERA40 input weather based on the output from each model. Table 1 shows temperature trends as absolute increases in magnitude relative to the 1980–2001 average, which we added to

Table 2. Ratios of precipitation rates in 2100 compared to 2001 from three models driven by IPCC scenario A1B (ratios in 2200 compared to 2001 appear in parentheses)

Month	High warming MIROC3.2	Medium warming HadCM3	Low warming CCSM3
Jan	1.53 (1.53)	1.58 (2.05)	1.36 (1.38)
Feb	1.62 (1.62)	1.49 (1.80)	1.28 (1.32)
Mar	1.50 (1.50)	1.46 (1.46)	1.28 (1.29)
Apr	1.40 (1.40)	1.46 (1.46)	1.18 (1.19)
May	1.26 (1.26)	1.18 (1.40)	1.15 (1.19)
Jun	1.19 (1.19)	1.18 (1.18)	1.13 (1.19)
Jul	1.18 (1.18)	1.21 (1.29)	1.16 (1.16)
Aug	1.19 (1.19)	1.25 (1.25)	1.13 (1.16)
Sep	1.24 (1.24)	1.21 (1.21)	1.19 (1.17)
Oct	1.56 (1.56)	1.31 (1.31)	1.28 (1.29)
Nov	1.65 (1.65)	1.48 (1.70)	1.24 (1.35)
Dec	1.60 (1.60)	1.61 (1.89)	1.36 (1.34)

Table 3. Ratios of incident short-wave radiation in 2100 compared to 2001 per month from three models driven by IPCC scenario A1B (ratios in 2200 compared to 2001 appear in parentheses)

Month	High warming MIROC3.2	Medium warming HadCM3	Low warming CCSM3
Jan	0.87 (0.87)	0.91 (0.90)	0.86 (0.86)
Feb	0.88 (0.88)	0.91 (0.91)	0.91 (0.91)
Mar	0.91 (0.91)	0.92 (0.92)	0.89 (0.89)
Apr	0.90 (0.90)	0.91 (0.91)	0.92 (0.92)
May	0.89 (0.89)	0.93 (0.93)	0.91 (0.91)
Jun	0.97 (0.97)	1.00 (1.00)	0.96 (0.96)
Jul	1.04 (1.04)	1.05 (1.05)	1.00 (1.00)
Aug	1.00 (1.00)	1.08 (1.08)	1.00 (1.00)
Sep	0.80 (0.80)	0.87 (0.87)	0.90 (0.90)
Oct	0.69 (0.67)	0.82 (0.79)	0.77 (0.77)
Nov	0.75 (0.75)	0.85 (0.85)	0.77 (0.77)
Dec	0.87 (0.87)	0.90 (0.90)	0.82 (0.82)

the ERA40 input temperatures. Values in parentheses show temperature increases in the 22nd century relative to the 21st century. Tables 2 and 3 show precipitation and short-wave radiation trends as ratios relative to average values from 1980 to 2001. The values in parentheses show the ratios in 2200 relative to the 1980–2001 average. We multiplied input ERA40 values by these ratios to scale precipitation and incident short-wave radiation.

We use one set of linear increases from 2002 to 2100 and a second set after 2100 because in the A1B scenario, the CO_2 concentrations are held constant at 700 ppm after 2100. However, air temperature and other variables will continue to change after this date as the climate stabilizes to new CO_2 levels. Simulations from HadCM3 are available to 2100, so for the 22nd century, we average the change rates from CCSM3 and MIROC3.2. In some months for some models, trends in precipitation and solar radiation after 2100 are not statistically significant at the 95% level. In these cases, scaling factors were held constant after 2100. We linearly interpolate the monthly change rates throughout the year to prevent any sudden jumps in temperatures between months. The scaling factors are piecewise continuous in time to preclude any sudden jumps in input weather variables as the slopes of the linear increases change in 2002 and 2100.

We scaled the input water vapour mixing ratio and atmospheric downwelling long-wave radiation proportional to temperature, assuming constant relative humidity and long-wave emissivity. For water vapour, we first calculated relative humidity using un-scaled temperature and water vapour mixing ratio. After scaling temperature, we calculated the new saturation vapour pressure and used the relative humidity to calculate a scaled water vapour mixing ratio. For long-wave radiation, we first calculated long-wave emissivity using un-scaled temperature and long-wave radiation in the Stefan–Boltzman equation. We then calculated the scaled long-wave flux using this emissivity and the scaled temperature, again using the Stefan–Boltzman equation.

We use a piecewise continuous function for atmospheric CO_2 concentrations: a fit to observed atmospheric CO_2 concentrations before 2002, a linear increase to 700 ppm from 2002 to 2100, then a constant CO_2 concentration of 700 ppm after 2100. For the past changes in atmospheric CO_2 concentration, we use a curve fit to observed global CO_2 concentrations from the ice core from Taylor Dome (Indermuhle et al., 1999) and the Globalview flask network (Masarie and Tans, 1995). To represent CO_2 concentrations from the A1B scenario, we linearly increase the global atmospheric CO_2 concentration to 700 ppm in 2100 then hold it constant at 700 ppm after 2100. To approximate seasonal variation of atmospheric CO_2 as a function of latitude, we superimpose observed seasonal variation from the Barrow, Mauna Loa, and South Pole flask sites onto the global average CO_2 concentrations. We linearly interpolate the seasonal cycle as a function of latitude. The resulting CO_2 concentrations match the observed global values and values from individual flask sites within 3–5 ppm.

We assume steady-state initial conditions in 1973 for soil temperature, soil moisture and carbon pools. Assuming steady-state is a useful way to initialize model prognostic variables in regions where we lack large-scale observations, such as Arctic permafrost. To achieve steady-state initial conditions, we ran SiBCASA for 4000 years by repeating the 1973–2001 multiyear block of ERA40 weather. At the start of spin-up (year zero), we assumed soil temperatures equal to the annual average air temperature with fully saturated soil moisture. Every 29 years during the first three spinup simulations, we algebraically calculated steady-state carbon pool sizes, which depend on soil temperature and moisture (Schaefer et al., 2008). The carbon pools, soil temperatures and soil moistures were allowed to vary freely for the last 3900 years of spinup.

Table 4. R_{pc} scaling factors for continuous permafrost (factors for discontinuous permafrost appear in parentheses)

R_{pc} scaling case	Code	Carbon density	Permafrost extent	Total
Low density – low permafrost	LDLP	0.75	0.9 (0.5)	0.68 (0.38)
Low density – high permafrost	LDHP	0.75	1.0 (0.9)	0.75 (0.68)
Med density – low permafrost	MDLP	1.0	0.9 (0.5)	0.90 (0.50)
Med density – high permafrost	MDHP	1.0	1.0 (0.9)	1.00 (0.90)
High density – low permafrost	HDLP	1.25	0.9 (0.5)	1.13 (0.63)
High density – high permafrost	HDHP	1.25	1.0 (0.9)	1.25 (1.13)

We define steady-state for soil moisture, soil temperature and ALT as less than 1% variability between consecutive spinup simulations. This resulted in a repeating pattern of inter-annual variability between 1973 and 2001 within 1% in soil moisture, soil temperature and ALT. For the carbon cycle, we define steady-state as carbon pool values such that respiration balances photosynthetic uptake within 1% from 1973 to 2001. Net Ecosystem Exchange (NEE) is respiration minus plant photosynthesis (a positive NEE indicates a net flux of CO_2 into the atmosphere). Steady-state indicates an average NEE between 1973 and 2001 within 1% of zero. Starting with these steady-state initial conditions, we then ran two projections from 1973 to 2200 for each of the three assumed warming rates, one with permafrost carbon and one without.

We calculate projected loss in permafrost area as the decrease in area with permafrost at the end of the projection (2180–2200) compared to the initial area with permafrost (1981–2001). We define the projected increase in ALT as the average ALT between 2180 and 2200 minus the average ALT from 1981–2001. A pixel contains permafrost if any soil layer is continuously at or below 0 °C for at least two consecutive years. The lower boundary of the soil model is set at 15 m depth, so the reduction in permafrost area means permafrost disappearance within the top 15 m of soil.

We calculate changes in the stock of frozen, permafrost carbon relative to the initial, steady-state value of 313 Gt in 2001. The permafrost carbon stock is the difference between D_{min} and D_{max} times the assumed permafrost carbon density of 21 kg C m^{-3}, multiplied by grid cell area and summed globally. We simulate an initial, steady-state amount of recent, 'unfrozen' carbon within the active layer of 91 Gt, for a total of 414 Gt of carbon in the top 3 m of soil. Tarnocai et al. (2009) estimate a total carbon content of 818 Gt in the top 3 m of soil for all permafrost regions. Our domain only includes continuous and discontinuous permafrost regions in the Northern Hemisphere, which Tarnocai et al. (2009) estimates to contain ~575 Gt of carbon (ignoring deposits below 3 m).

2.3. *PCF strength and timing*

We define PCF strength in terms of total heterotrophic respiration flux of thawed permafrost carbon (R_{pc}). R_{pc} is the difference in NEE between the simulations with and without permafrost carbon. R_{pc} is the total emissions of old carbon from thawing permafrost, excluding all fluxes of more recent carbon from the active layer. R_{pc} is a surrogate for a more accurate estimate of PCF strength in terms of the difference in surface radiative forcing with and without the PCF, accounting for interactions with other carbon and climate feedbacks. This, however, requires using a fully coupled land–ocean–atmosphere General Circulation Model, which is beyond the scope of this project. Defining PCF strength in terms of R_{pc} does allow direct comparison with other global atmospheric carbon sources and sinks.

To estimate the start of the PCF, we define a starting point as the year when the cumulative R_{pc} summed from the start of the simulation permanently exceeds a threshold representing natural background variability in NEE. The starting point indicates when the permafrost carbon has begun to thaw and decay. The threshold is set at plus three standard deviations above the 1973–2001 average in cumulative NEE. Using cumulative R_{pc} and NEE removes high background noise due to normal inter-annual variability, making the starting point much easier to detect. Defining the threshold relative to 1973–2001 variability in cumulative NEE ensures that the starting point occurs only when R_{pc} exceeds natural background variability in net carbon flux. If the cumulative R_{pc} subsequently falls below the threshold, the PCF starting point is reset to a default value of 2200.

2.4. *Uncertainty*

Our estimates of PCF strength quantify uncertainty due to (1) the assumed warming rate, (2) the assumed permafrost carbon density and (3) the fraction of permafrost extent within a grid cell. We use a simple R_{pc} scaling strategy to estimate the maximum envelope of uncertainty because running a large number of simulations in a Monte Carlo framework to statistically assess uncertainty is beyond the scope of this project. We estimate R_{pc} for six ensemble members for each assumed warming rate, with each member assuming a different permafrost carbon density and subgrid permafrost extent, creating a total of 18 R_{pc} ensemble members. The ensemble mean represents our best estimate of the PCF strength, and the standard deviation of all ensemble members represents our estimate of uncertainty.

We assume three values of permafrost carbon density representing typical values reported in the literature: 15.75, 21.0 and

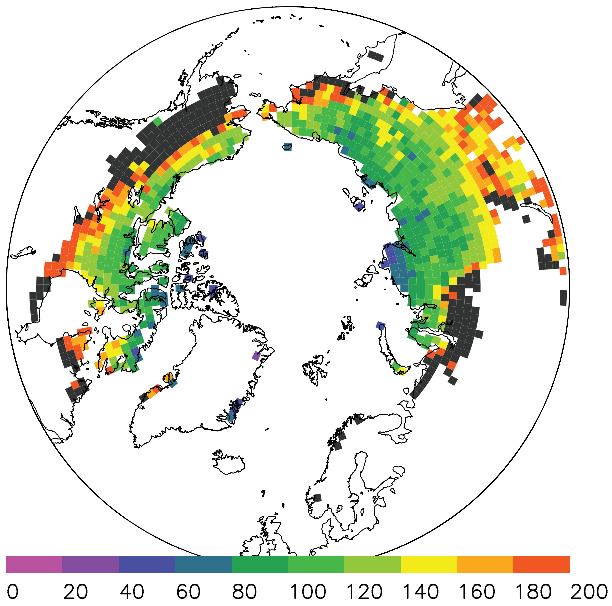

Fig. 3. A map of mean simulated active layer thickness (ALT) from 1973 to 2001 (cm). Black pixels are regions where SiBCASA did not simulate permafrost.

26.26 kg m^{-3}. This effectively assumes a 25% uncertainty in the total simulated permafrost carbon pool, or 313 ± 78 Gt of frozen carbon in the top 3 m of soil. In continuous permafrost regions, permafrost covers 90–100% of the land area, while in discontinuous permafrost regions, permafrost covers 50% to 90% the land area (Brown et al., 1998; Zhang et al., 1999). Maximum permafrost extent assumes 100% coverage in continuous permafrost and 90% coverage in discontinuous permafrost. Minimum permafrost extent assumes 90% coverage in continuous permafrost and 50% in discontinuous permafrost.

Table 4 shows the permafrost carbon density, subgrid permafrost extent and total R_{pc} scaling factors for each warming rate. To estimate, for example, R_{pc} for low carbon density and low permafrost extent (LDLP) in continuous permafrost, we multiply the un-scaled R_{pc} by 0.45. For high carbon density and high permafrost extent (HDHP) we multiply R_{pc} by 1.5, etc. Scaling factors for discontinuous permafrost appear in parentheses. This simple scaling is possible because R_{pc} varies linearly with the assumed permafrost carbon density (not shown). To convert back to NEE we add these scaled R_{pc} estimates to the average NEE from the simulations without permafrost carbon.

3. Results

3.1. *Simulated permafrost*

After spinup, SiBCASA simulated permafrost in 79% of continuous and discontinuous permafrost regions (Fig. 3). The black areas in Fig. 3 are regions where SiBCASA simulated no permafrost after spinup. SiBCASA was able to simulate permafrost in 91% of continuous permafrost, but only 41% of discontinuous permafrost, which covers 26% of our domain along the southern margins. SiBCASA cannot capture the small-scale processes that drive subgrid heterogeneity in permafrost extent, so each grid cell is binary: either all permafrost or no permafrost. SiBCASA often did not simulate permafrost in discontinuous permafrost regions where permafrost covers only 50–90% of the grid cell area. These regions formed talik at the start of spinup, which eventually expanded to thaw the entire 15 m soil column after 4000 years of spinup. We assumed permafrost carbon extended only down to 3 m depth, so regions where SiBCASA did not simulate permafrost did not contribute to the PCF.

After spinup, simulated ALT were 80–90% of observed values in the Siberian interior, but nearly double observed values along the Arctic coastline (Fig. 3). We compared simulated ALT with observed values from the Circumpolar Active Layer Monitoring network (Brown et al., 2000) and the Russian Soil Temperature network (Zhang et al., 2005). The ALT bias along the Arctic coastline results from a positive bias in incident, down-welling short-wave radiation in the ERA40. In the Siberian interior, trees in SiBCASA absorbed the excess energy with minimal effect on simulated ALT. On the treeless tundra along the Arctic coastline, however, the excess energy was absorbed by the ground, resulting in simulated ALT greater than observed. However, the simulated year-to-year variability and long-term trends matched observed values.

3.2. *Permafrost degradation*

We project a 53–97 cm average increase in ALT and a 29–59% decrease in permafrost extent by 2200. Figure 4 shows the projected increases in ALT by 2200 from the SiBCASA simulation driven by HadCM3 (medium warming rate). The black regions in Fig. 4 indicate where SiBCASA simulated no permafrost after spinup and the ALT is undefined. The red regions in Fig. 4 along the southern margin of the permafrost domain indicate the loss of permafrost between 2002 and 2200. For the HadCM3 (medium warming) simulation, the average ALT increase in regions that retain permafrost is 83 ± 24 cm with a 50% reduction in permafrost area by 2200. The CCSM3 (low warming) simulation shows smaller ALT increases of 53 ± 17 cm with a smaller, 29% decrease in permafrost area. The MIROC3.2 (high warming) simulation shows the largest ALT increases of 97 ± 22 cm with a larger, 59% decrease in permafrost extent.

All pixels showed a similar progression of degradation with talik thickness exceeding a critical threshold initiating rapid thaw of the soil column. As air temperatures rose over time, the ALT and permafrost temperatures increased. Eventually, the permafrost temperatures just below the active layer would approach 0 °C and the bottom of the active layer would only partially freeze each winter, forming a talik. Once the talik expanded beyond a critical thickness, the soil column became thermodynamically unstable and thawed rapidly, with simulated thaw rates

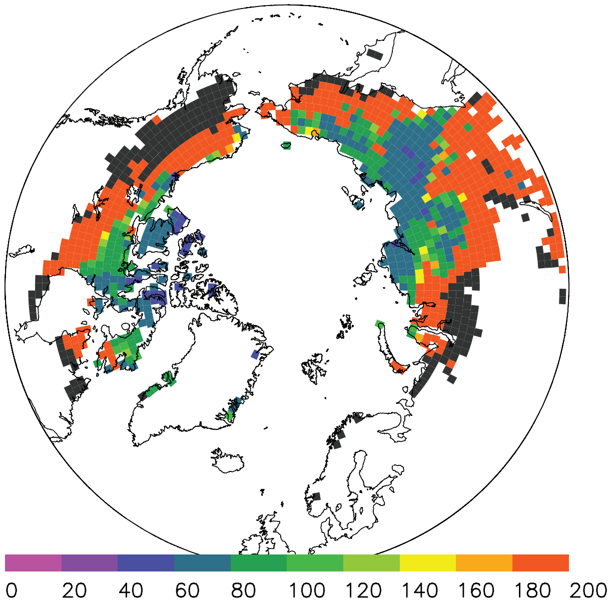

Fig. 4. Simulated increases in active layer thickness (ALT) by 2200 (cm) for the medium warming simulation. Black regions have no permafrost in 2001. Red regions show loss of permafrost by 2200.

often exceeding 100 cm decade^{-1}. New talik formation stopped after the warming stopped in 2100, but pixels with talik exceeding the critical thickness continued to rapidly thaw until the loss of permafrost extent abruptly slowed in 2120. After 2120, pixels containing thick talik formations continued to thaw, but at greatly reduced rates indicating a slow decline in permafrost extent well after our simulations stopped in 2200.

The loss of permafrost extent started at the southern margins and progressed northward, contracting around permafrost regions with the coldest temperatures. For all three warming rates, permafrost disappeared first along the southern margins because warmer temperatures make these regions more vulnerable to degradation (Zhang et al., 2008a,b). First, talik appeared along the southern margins of permafrost regions. Then, as the talik expanded over time and the permafrost thawed, the southern margin of permafrost regions moved northward. The southern margin of the remaining permafrost contracted around those areas with the coldest temperatures. These areas thaw last because they are the coldest regions in the Arctic and thus are most resistant to thaw due to warming. Regions that are most resistant to thaw are easily identified as having the smallest increases in ALT in Fig. 4: North-Central Siberia and the islands of Northeast Canada.

Our projections of permafrost degradation fall on the low side, but well within the range of other published projections. Table 5 shows the decrease in permafrost area and the increase in ALT for this study compared to other published projections of permafrost degradation. All these projections end in 2100 and have different domains, so we calculated our estimated decrease in permafrost area and increase in ALT by 2100 for domains that correspond to each published projection (last three lines in Table 5). For some projections, we calculated the percent decreases in permafrost area from tables or values of absolute decreases in area. We listed the projections in order of increasing estimated permafrost degradation. Two of the published projections show less degradation than we predict, five projections show greater degradation, and two overlap. Although the magnitude of area decrease and ALT increase varies widely, all of these projections show the same spatial pattern of permafrost degradation over time: loss of permafrost starting from the southern margins and progressing northward, with remnants in Northeast Canada and Central Siberia.

The large spread in estimated permafrost degradation between these projections may result from the assumed IPCC scenarios, the strength of land atmosphere feedbacks and model structural differences. Lawrence and Slater (2005), for example, show that the lower warming rate in the B1, low emission scenario results in only a 60% reduction in permafrost extent, compared to 90% for the A2, high emission scenario. The strength or inclusion of various land–atmosphere feedbacks and associated surface warming varies from model to model, resulting in different estimates of permafrost degradation. Differences in model internal structure, particularly in the snow model, will produce different degradation rates. Thermal conductivity increases with snow density, so simulated snow depth and density combined determine the overall insulating effect of snow pack on the soil thermal regime (Ling and Zhang, 2004; Zhang et al., 2005). How models represent snow compaction processes will influence snow thermal conductivity and thus permafrost degradation. Quantifying how these and other factors might control projected permafrost degradation requires a detailed model-to-model comparison that is beyond the scope of this study.

3.3. PCF dynamics

Before exploring the global effects of the PCF, let us first examine a single point in detail to understand the basic dynamics of permafrost carbon thaw and decay. Figure 5 shows the increase over time of ALT, cumulative NEE, and cumulative permafrost carbon flux, R_{pc}, at a continuous permafrost location in central Siberia (63°N, 130°E). As seen in Fig. 5a, the ALT increases after the warming starts in 2002. A talik forms in 2080 and expands at a rate of 100 and 200 cm decade^{-1} for the medium and high warming rates, respectively. By 2200, the entire soil column thaws for the high warming rate. For the medium warming rate, talik expansion abruptly slowed after 2120 with complete thaw out to occur some time after 2200. For the low warming rate, the ALT steadily increased until 2120 and then stabilized with an ALT increase of ~54 cm.

Permafrost carbon starts to thaw when ALT first exceeds D_{min} and stops thawing when either ALT stops increasing or ALT exceeds D_{max}. ALT is highly variable such that D_{min} does not increase smoothly and continuously, but in sudden jumps in

Table 5. Decrease in permafrost area and increase in active layer depth (ALT) in 2100 for this study compared to other published projections of permafrost degradation

Study	Scenario (s)	Domain	Decrease in permafrost area (%)	Increase in ALT (cm)
Marchenko et al. (2008)	A1B	Alaska	7.0[a]	162[b]
Zhang et al. (2008a)	B2, A2	Canada	16–20[a]	30–70
Zhang et al. (2008b)	B2, A2	Canada	21–24	30–80
Euskirchen et al. (2006)	A1B	No. Hem.	27[a]	–
Saito et al. (2007)	A1B	Northern Hemisphere	40–57	50–300
Lawrence and Slater (2005)	A2, B1	Northern Hemisphere	60–90	50–300
Eliseev et al. (2009)	B1, A1B, A2	Northern Hemisphere	65–80[a]	100–200
Lawrence and Slater (2010)	A1B	Northern Hemisphere	73–88	–
Lawrence et al. (2008)	A1B	Northern Hemisphere	80–85	50–300
This Study	A1B	Alaska	22–61	69–105
This Study	A1B	Canada	22–36	55–90
This Study	A1B	Northern Hemisphere	20–39	56–92

[a]Calculated from numbers or tables in text.
[b]Calculated from estimated trends.

particularly warm years. Consequently, the permafrost carbon is thawed and shifted to the active soil carbon pools in a series of large clumps rather than a continuous trickle over time. For all three warming rates, the permafrost carbon starts to thaw in 2026, when the ALT first exceeds D_{min} to thaw ~20 cm of permafrost carbon. This carbon periodically freezes and thaws until 2060, where we see another large jump in ALT and D_{min}. For the medium and high warming rates, all the permafrost carbon is thawed when the ALT exceeds D_{max} in 2107 and 2086, respectively. For the low warming rate, ALT never exceeds D_{max} and 54% of the initial stock of frozen carbon is thawed by 2200 (49% before 2100 and 5% after 2100). For all three warming rates, the thawing of permafrost carbon starts in 2026 and effectively stops by 2100.

Accounting for the thaw and decay of permafrost carbon changes this site from a sink to a source relative to the atmosphere. The cumulative NEE in Fig. 5b start near zero for all simulations, as expected assuming steady-state initial conditions. A positive NEE indicates a net carbon flux into the atmosphere. Fluctuations in cumulative NEE prior to 2002 vary between −0.07 and 0.26 kg C m^{-2} with a PCF starting point threshold of 0.27 kg C m^{-2}, consistent in magnitude with observed cumulative fluxes for a spruce forest in Manitoba (Dunn et al., 2007). After 2001, the cumulative NEE turns negative, indicating a build-up of terrestrial carbon driven by enhanced photosynthetic uptake. Warmer temperatures simultaneously increase soil respiration and photosynthetic uptake, but the effect of photosynthetic uptake is stronger, resulting in a net carbon sink. After 2026, the cumulative NEE with permafrost carbon shift upward, indicating that the thawed permafrost carbon has begun to decay. The starting point for this site is 2033 ± 2 years, when R_{pc} from thawed permafrost carbon increases beyond natural background variability in NEE, resulting in a net carbon source relative to the atmosphere.

The decay of thawed permafrost carbon is slow and continues long after the thawing stops (Fig. 5c). Although 'thawed', the soil is still cold and often refreezes each year, resulting in a relatively slow decay of permafrost carbon. Nearly all the permafrost carbon thawed out before 2100, but 43% of cumulative R_{pc} occurred after 2100. The permafrost carbon decays with a characteristic e-folding time of ~70 years such that the slope of the cumulative R_{pc} curve slowly decreases over time. When additional carbon is thawed, the slope of the cumulative R_{pc} curve abruptly increases, producing a characteristic wave pattern. At this site, D_{min} increases and associated transfers from the permafrost carbon pool started in 2026 and occurred every 20–30 years, resulting in a weak wave pattern. The uncertainty in R_{pc} varies between 31% and 45%, mainly due to differences in when the permafrost carbon thawed between the three warming rates. By 2200, the R_{pc} curve flattens out and 90% of the thawed permafrost carbon has decayed away and has been released into the atmosphere.

3.4. *PCF strength*

The pan-Arctic, cumulative NEE without the effects of permafrost carbon indicate a continual build-up of carbon in the terrestrial biosphere (lower three curves in Fig. 6). Without permafrost carbon, we estimate a cumulative, pan-Arctic sink of 33–46 Gt C in 2100, which is comparable the ~35 Gt estimated by Qian et al. (2010) based on the ensemble mean of 10 models in the Coupled Carbon Cycle Climate Model Intercomparison Project. After 2100, the A1B IPCC scenario keeps CO_2 concentrations constant at 700 ppm, resulting in much lower warming rates as the climate stabilizes at the higher CO_2 concentration. However, the terrestrial build-up of carbon continues due to wood growth. The longer growing seasons, warmer temperatures and higher atmospheric CO_2 promote wood growth in the forested permafrost regions of southern Siberia and, to a lesser

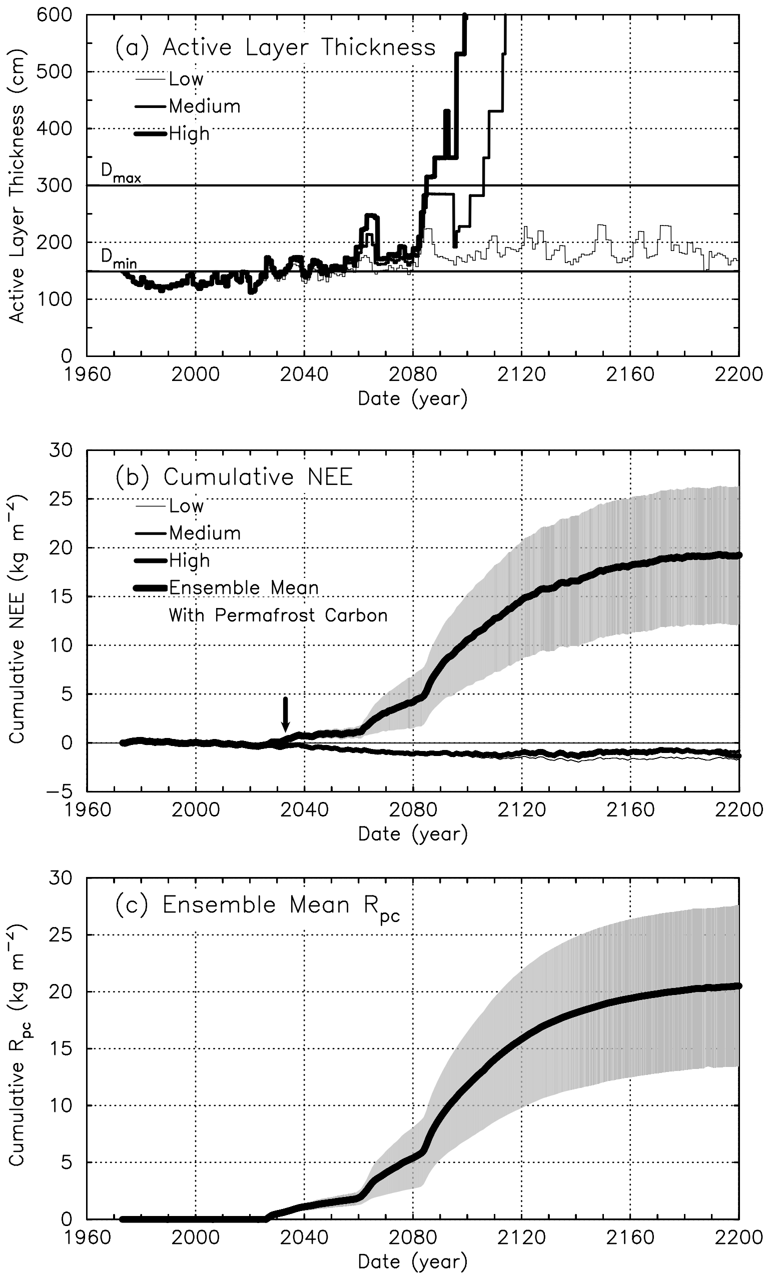

Fig. 5. Typical carbon fluxes for a point in central Siberia (63°N, 130°E) showing (a) changes in active layer thickness (ALT) for low, medium and high warming rates; (b) cumulative Net Ecosystem Exchange (NEE) for low, medium and high warming rates without permafrost carbon and the ensemble mean with permafrost carbon and (c) ensemble mean cumulative permafrost carbon flux (R_{pc}). A positive NEE indicates a net release of carbon into the atmosphere. The arrow in (b) indicates the starting point of 2033 ± 2 years.

extent, the boreal permafrost regions of North America. The sink persists because the soil and litter pools, and associated heterotrophic respiration, cannot reach steady-state until the wood pool reaches equilibrium (Schaefer et al., 2008). After 2120, the cumulative NEE without permafrost carbon curves have begun to flatten, indicating SiBCASA is approaching steady-state. However, with wood turnover times of 30–50 years, SiBCASA would not reach steady-state NEE until ∼2400.

Accounting for the PCF changes the permafrost regions from a net carbon sink to a net source relative to the atmosphere. The upper line in Fig. 6 shows the NEE that would result when including the ensemble mean of R_{pc}, with the grey-shaded region indicating uncertainty. The cumulative NEE curve with permafrost carbon is smoother and more gradual than the single point curve shown in Fig. 5b because it represents the average of many grid cells with varying degrees of degradation. The starting point when the pan-Arctic R_{pc} exceeds background variability in NEE is 2023 ± 4 years, as indicated by the arrow in Fig. 6. The relative uncertainty in R_{pc} is ∼35%, but even with this large uncertainty, the cumulative NEE is well above zero, indicating a net source of carbon relative to the atmosphere.

The largest source of uncertainty in PCF strength, in terms of cumulative R_{pc}, is the assumed warming rate and, to a lesser extent, the assumed permafrost carbon density. Fig. 7 shows the cumulative, pan-Arctic R_{pc} for all 18 ensemble members, grouped by low, medium, and high warming rates for clarity. The low warming rate produces the least amount of thaw, the lowest R_{pc}, and the weakest PCF. Conversely, the high warming rate produces the greatest amount of thaw, the highest R_{pc}, and the strongest PCF. Overlap or similarity in R_{pc} between ensemble members indicates equifinality between assumed warming rate, permafrost carbon density, and permafrost extent. Equifinality means that multiple combinations of values for two or more parameters can produce the same model output. Low warming rates with high permafrost carbon density can produce the same R_{pc} as high warming rates with low permafrost carbon density. The spread between ensemble members, and thus overall R_{pc} uncertainty, is dominated by uncertainty in the warming rate and the assumed permafrost carbon density.

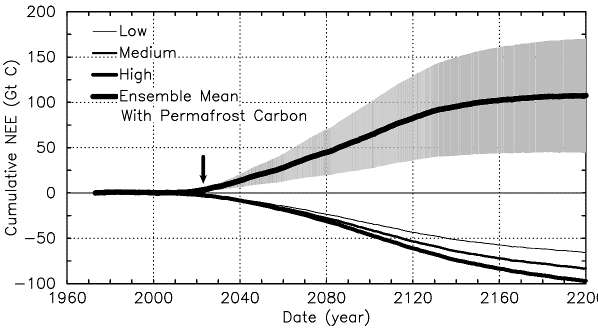

Fig. 6. Pan-Arctic total cumulative Net Ecosystem Exchange (NEE) for low, medium and high warming rates without permafrost carbon and the ensemble mean cumulative NEE with permafrost carbon flux. The grey bar represents uncertainty and the arrow marks the pan-Arctic starting point of 2023 ± 4.

Our best estimate of PCF strength indicates a cumulative flux of 190 ± 64 Gt of permafrost carbon to the atmosphere by 2200 (Fig. 7d). This corresponds to an overall release into the atmosphere of 61 ± 20% of our initial 313 Gt of frozen carbon. Like the single point example above, 80–90% of the thawing of permafrost carbon occurs before 2100, but 46% of the thawed carbon is released into the atmosphere after warming stops in 2100. The 'thawed' permafrost carbon sits at the bottom of a cold active layer or in cold soil that often refreezes each winter, resulting in slow microbial decay. We find characteristic e-folding times for microbial decay of ~70 years, indicating that the release of permafrost carbon to the atmosphere continues for some time after atmospheric warming stops. Even with this slow rate of microbial decay, our results indicate that more than 90% of the thawed permafrost carbon is released into the atmosphere by 2200. This suggests that future climate scenarios and model runs need to extend beyond 2100 to assess the impact of changing climate on the carbon cycle.

We almost certainly underestimate total R_{pc} because our simulations exclude permafrost regions along the southern margins where SiBCASA did not simulate permafrost. SiBCASA did not simulate permafrost in 59% of discontinuous permafrost representing 14% of the entire domain, so these regions do not contribute to R_{pc}. However, in discontinuous regions where

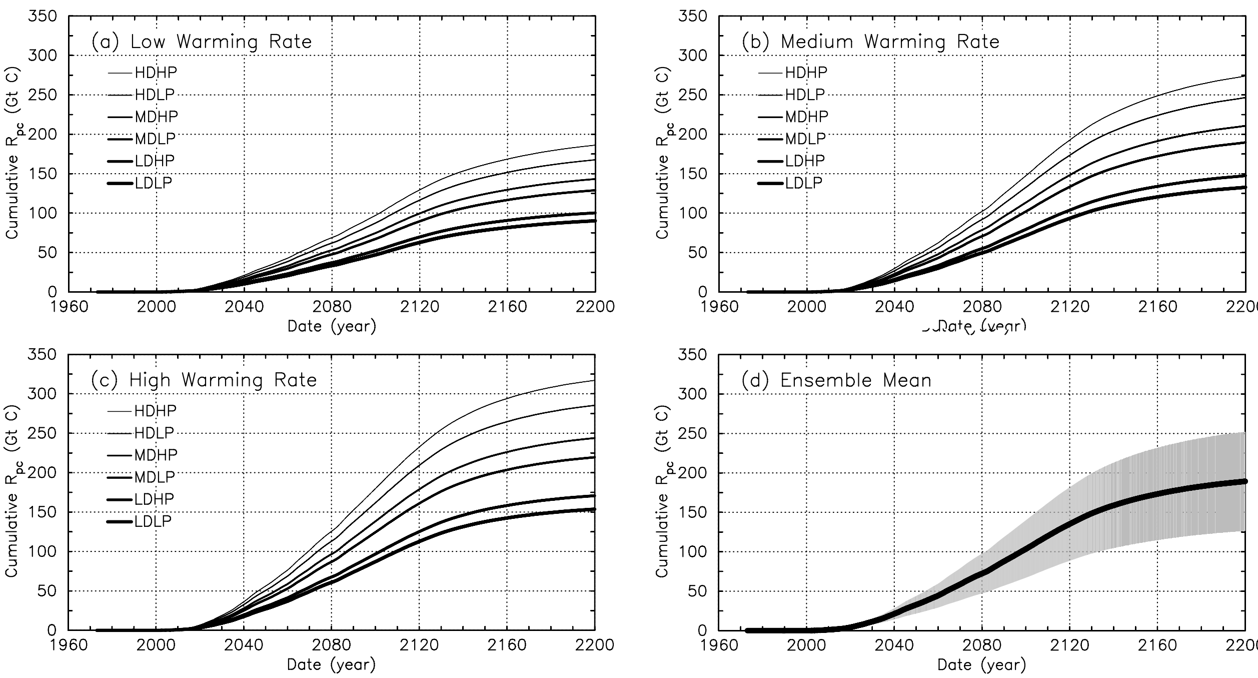

Fig. 7. Ensemble members of cumulative permafrost carbon flux (R_{pc}) for continuous and discontinuous permafrost for (a) low warming rate, (b) medium warming rate, (c) high warming rate and (d) ensemble mean ± 1 *SD*. Line labels correspond to the ensemble member codes in Table 4.

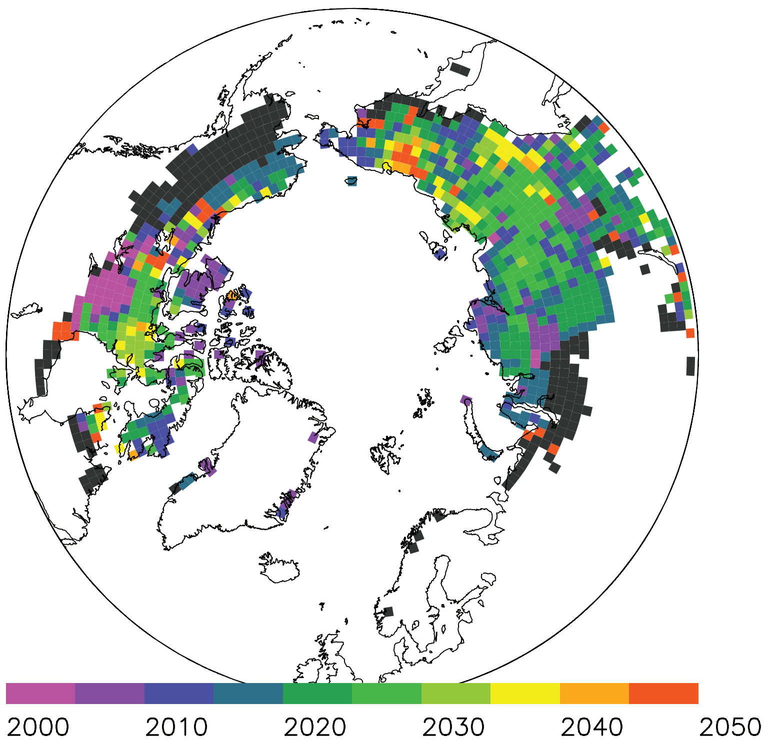

Fig. 8. Map of permafrost carbon feedback (PCF) starting points based on the permafrost carbon flux (R_{pc}) ensemble mean. Black regions have no permafrost in 2001 with zero R_{pc} and undefined starting points.

SiBCASA did simulate permafrost, 92–99% of the frozen carbon thawed out and nearly all of it before 2060. Discontinuous permafrost regions where SiBCASA did not simulate permafrost are equally or perhaps more vulnerable to thaw, indicating our estimated R_{pc} is biased low.

3.5. *PCF timing*

Fig. 8 shows a map of starting points indicating the year when ALT increases beyond natural background variability to thaw sufficient permafrost carbon such that R_{pc} increases beyond natural background noise in NEE. Black regions indicate where SiBCASA did not simulate permafrost, R_{pc} is zero, and the starting point undefined. The scattered red pixels along the southern margins indicate locations with very little initial permafrost carbon (initial D_{min} very close to D_{max}) such that cumulative R_{pc} is smaller than NEE variability and a starting point does not occur.

Spatial variability in starting points is driven by the projected ALT increase relative to the background variability in ALT. Generally speaking, the greater the increase in ALT, the earlier the starting point. Where increases in ALT are fairly small (such as North-Central Siberia and Northeast Canada) inter-annual variability in ALT modulates the starting point. Some regions along the Arctic coastline have relatively small inter-annual variability in ALT, so a smaller amount of warming can increase the ALT beyond background variability, resulting in early starting points.

Our results indicate a pan-Arctic PCF starting point some time in the mid-2020s. Ignoring points with undefined starting points, the earliest starting point is 2002 and the latest is 2061. This means that permafrost carbon will begin to thaw everywhere by 2061. The average starting point is 2024 and a standard deviation of ±27 years. The pan-Arctic fluxes in Fig. 6 indicate a pan-Arctic starting of 2023 ± 4 years based on the total R_{pc} from all continuous and discontinuous regions.

Some regional starting points are biased early, indicating the global starting point may be biased early as well. Several regions reach starting points before 2010, but there is no observational evidence indicating that these regions have, in fact, released permafrost carbon into the atmosphere. The most obvious example is the region west of Hudson Bay in Canada, which reached a starting point of 2002 for all three warming rates. This region appears as a bright purple spot with starting points before 2005 in Fig. 8. This indicates that in some regions, such as west of Hudson Bay, we may have underestimated D_{min} and overestimated cumulative R_{pc} in the early part of the 21st century, resulting in an early bias for the pan-Arctic starting point.

Regions along the southern margins where the starting point occurs before 2020 are candidate regions where we might first measure and detect R_{pc}, and thus monitor the start of the PCF. Early detection of R_{pc} is unlikely in regions where the starting point occurs after 2020, such as Northeast Canada and North-Central Siberia. Regions where SiBCASA did not simulate permafrost are also vulnerable to thaw and are likely areas where we could detect R_{pc}. Knowledge of which regions might thaw first can help guide an overall strategy to measure R_{pc} and thus monitor the PCF.

4. Discussion

4.1. Comparison to other sources and sinks

A cumulative R_{pc} of 190 ± 64 Gt C by 2200 is equivalent to an increase in atmospheric CO_2 concentration of 87 ± 29 ppm, which is consistent with increases after glacial terminations assessed from the Vostok ice core (Petit et al., 1999). To convert permafrost carbon flux to equivalent changes in atmospheric CO_2 concentration, we assumed 0.4608 ppm Gt^{-1} of carbon, ignoring other climate–carbon cycle feedbacks. The Vostok record shows increases of ∼80 ppm associated with 8–10 °C increases in global temperature after glacial terminations. In our simulation, the annual average air temperature increased by 1.1–1.7 °C before reaching the starting point of 2024, consistent in magnitude with the observed 1.0–1.5 °C temperature increases before atmospheric CO_2 concentrations begin to rise (Petit et al., 1999). Our simulations show much of the permafrost carbon flux occurs after the warming stops, creating a lag of about 100 years between the start of warming and the expected rise in atmospheric CO_2. The Vostok record also shows that increases in atmospheric CO_2 concentration lag behind increases in temperature by 600 ± 400 years (Fischer et al., 1999). Much of the increase in atmospheric CO_2 after glacial termination is attributed to ocean fluxes. However, we speculate that the lag behind temperature and some of the observed CO_2 increases may result from the thaw of permafrost carbon.

The PCF is strong compared to projections of the total terrestrial land sink. The cumulative projected global land carbon sink is ∼160 Gt C by 2100, driven by enhanced photosynthetic uptake in the tropics due to increased atmospheric CO_2 concentrations (Friedlingstein et al., 2006). We estimate a cumulative R_{pc} of 104 ± 37 Gt C in 2100, which is equivalent to 65 ± 23% of the projected global land carbon sink. What will happen after 2100 is uncertain because the projected global land carbon sink is not stable: if CO_2 concentrations were to level off or respiration in the tropics were to increase due to warmer soils, the global land carbon sink would weaken and eventually disappear.

Accounting for the PCF will require larger reductions in fossil fuel emissions to reach a target atmospheric CO_2 concentration and associated global climate. Like the burning of fossil fuels, the PCF injects old carbon buried on geologic time scales back into the atmosphere. Also like fossil fuels, the PCF is irreversible: once the permafrost carbon thaws and decays, no process on human time scales can put the carbon back into the permafrost. If any international strategy to reduce fossil fuel emissions does not account for the PCF, we will overshoot our desired atmospheric CO_2 concentration and end up with a warmer climate than intended. In the A1B scenario used in our simulations, the target CO_2 concentration is 700 ppm, placing the upper limit on total future carbon emissions at 1345 Gt (assuming ocean and terrestrial sinks persisting at 50% of emissions). This includes both fossil fuels and permafrost carbon, so with 190 ± 64 Gt of carbon from thawing permafrost, the limit on fossil fuel emissions is actually 14 ± 5% lower or 1157 ± 57 Gt C.

4.2. Other sources of uncertainty

Like many other models, SiBCASA has difficulty representing subgrid scale processes, introducing additional uncertainty in our estimates. SiBCASA cannot capture thermokarst development, river and coastal erosion, thaw lake hydrology and other subgrid scale processes that influence the rate of permafrost degradation (Walter et al., 2006; Schuur et al., 2008). Our estimate of PCF strength did not include the 21% of our domain where SiBCASA cannot capture subgrid heterogeneity in permafrost extent, primarily in discontinuous permafrost regions. Such discontinuous permafrost regions are vulnerable to thaw, implying greater permafrost carbon flux and a stronger PCF than we estimate. Only high-resolution simulations will solve this problem, but the lack weather driver data sets and greatly increased computational demands make such simulations almost impractical for 200-year projections.

We did not include permafrost carbon deposits below 3 m, indicating our estimates of R_{pc} may be biased low. Frozen carbon is found below 3 m in the Yedoma deposits of Siberia and deltaic deposits of the major Arctic rivers. Including deposits below 3 m would increase R_{pc} in regions where permafrost completely thaws out. Observations of the location, depth and carbon content of permafrost carbon deposits below 3 m are extremely scarce. Nevertheless, Tarnocai et al. (2009) estimate these deep deposits contain 648 Gt of carbon, indicating the bias in our estimated R_{pc} could be quite large.

Accounting for various feedbacks with other components of the climate system could either strengthen or weaken the PCF. The release of nutrients from the decay of permafrost carbon would increase net uptake in the nitrogen-limited Arctic ecosystems, partially off-setting R_{pc} and delaying the PCF starting point. The transport of thawed organic matter in rivers to the ocean for ultimate re-burial in sediments would weaken the PCF. Our off-line simulations do not account for amplified surface warming due to the PCF itself, which would promote further permafrost thaw and strengthen the PCF.

Other sources of uncertainty include the IPCC scenario, model structure and methane emissions. Different IPCC scenarios produce different warming rates and associated permafrost degradation, resulting in greater uncertainty in estimated R_{pc}. Processes that SiBCASA does not model introduce uncertainty in our results. For example, SiBCASA only approximates the processes that bury and release permafrost carbon on geologic time scales: cryoturbation, soil deposition, etc. SiBCASA does not include a wetland model and cannot evaluate how peatlands, changing lake hydrology and methane emissions will influence the PCF. Uncertainty in how SiBCASA represents physical processes, particularly snow processes, introduces uncertainty in our PCF projections.

5. Conclusions

Accounting for the PCF will require larger reductions in fossil fuel emissions to reach a desired atmospheric CO_2 concentration and associated climate. The PCF is strong enough to warrant inclusion in all projections of future climate. Our best estimate of PCF strength is 190 ± 64 Gt C of permafrost carbon released into the atmosphere by 2200. This estimate is probably low because it does not account for amplified surface warming due to the PCF itself and excludes some regions where SiBCASA was unable to simulate permafrost. About 61 ± 20% of the initial 313 Gt of frozen carbon in our simulations was released into the atmosphere with a potential to increase atmospheric CO_2 concentrations by 87 ± 29 ppm. We estimate a pan-Arctic PCF starting point in the mid-2020s when R_{pc} exceeds background variability in NEE, indicating some regions may already be releasing permafrost carbon to the atmosphere. The assumed warming rates and permafrost carbon density dominate our uncertainty estimate of ±64 Gt C in PCF strength (±35%). Even with this broad range of uncertainty, our modelling experiments highlight several important features of the PCF.

First, the strength of the PCF depends on the amount of projected permafrost degradation. The loss of permafrost will start at the southern margins of the permafrost domain and advance north, contracting around regions with the coldest temperatures: Northeast Canada and North-Central Siberia. A larger loss of permafrost extent means that a larger fraction of the initial permafrost carbon stock is thawed, resulting in proportionally higher R_{pc} in 2200. For 100% loss of permafrost extent or complete thaw-out of all permafrost, the entire initial stock of permafrost carbon would thaw, placing a theoretical upper limit on R_{pc} of ~300 Gt in 2200. By 2200, we project a 29–59% decrease in area containing permafrost, well within the range of previously published estimates. Other models that predict similar permafrost degradation will also predict a similar strength PCF.

Secondly, once initiated, the PCF is irreversible and strong compared to other global sources and sinks of atmospheric CO_2, even with large uncertainties. The PCF is strong enough to cancel enhanced uptake, changing the Arctic from a sink to a source of atmospheric CO_2. Our estimates of cumulative permafrost carbon flux to the atmosphere are equivalent to 42–88% of the estimated cumulative global land sink. Even with a broad range of uncertainty, the permafrost carbon flux to the atmosphere is large compared to projected fossil fuel emissions.

Finally, the release of permafrost carbon will continue for many years even if atmospheric warming stops. Permafrost has huge thermal inertia, resulting in a lag between when warming starts and thaw begins. The start of permafrost thaw typically occurred 25 or more years after warming started and 20% of the total thawing occurred after warming stopped in 2100. The models driven by the A1B scenario, none of which included the PCF, all stabilize at a new, warmer climate after 2100 when CO_2 concentrations level out at 700 ppm. However, our simulations indicate that the global carbon cycle will not stabilize until at least 2200. Nearly all thawing of permafrost carbon occurred before 2100, but 46% of permafrost carbon flux occurred after 2100. Once thawed, the permafrost carbon can take 70 years or more to decay due to cold soil temperatures and periodic refreezing. This slow response means that once the PCF starts, it will continue for a long time.

6. Acknowledgments

This study was in part supported by the U.S. National Aeronautics and Space Administration (NASA) grant NNX06AE65G as part of the North American Carbon Program, the U.S. National Oceanic and Atmospheric Administration (NOAA) Grant NA07OAR4310115, the U.S. NOAA Grant NOAA NA09OAR4310063 and the U.S. National Science Foundation (NSF) Grant ARC 0901962 to the University of Colorado at Boulder.

References

Anisimov, O. A. 2007. Potential feedback of thawing permafrost to the global climate system through methane emission. *Env. Res. Lett.* **2**, doi:10.1088/1748-9326/2/4/045016.

Ball, J. T. 1988. *An Analysis of Stomatal Conductance*, PhD Thesis, Stanford University.

Bonan, G. B. 1996. A Land Surface Model (LSM Version 1.0) for ecological, hydrological, and atmospheric studies: technical description and users guide. NCAR Technical Note NCAR/TN-417+STR, Boulder, Colorado.

Brown, J., Ferrians Jr., O. J., Heginbottom, J. A. and Melnikov, E. S. 1998. *Circum-Arctic Map of Permafrost and Ground-Ice Conditions* (revised February 2001). National Snow and Ice Data Center/World Data Center for Glaciology, Boulder, CO, Digital Media.

Brown, J., Hinkel, K. M. and Nelson F. E. 2000. The circumpolar active layer monitoring (CALM) program: research designs and initial results. *Polar Geog.* **24**, 165–258.

Cheng, G. and Wu, T. 2007. Responses of permafrost to climate change and their environmental significance, Qinghai-Tibet Plateau. *J. Geophys. Res.* **112**, doi:10.1029/2006JF000631.

Collatz, G. J., Ball, J. T., Grivet, C. and Berry, J. A. 1991. Physiological and environmental regulation of stomatal conductance, photosynthesis, and transpiration: a model that includes a laminar boundary layer. *Agric. Forest Meteorol.* **54**, 107–136.

Collatz, G. J., Ribascarbo, M. and Berry, J. A. 1992. Coupled photosynthesis-stomatal conductance model for leaves of C4 plants. *Aust. J. Plant Physiol.* **19**, 519–538.

Cramer, W., Bondeau, A., Woodward, F. I., Prentice, I. C., Betts, R. A., and co-authors. 2001. Global response of terrestrial ecosystem structure and function to CO2 and climate change: results from six dynamic global vegetation models. *Global Change Biol.* **7**, 357–373.

Dai, Y., Zeng, X., Dickinson, R. E., Baker, I., Bonan, G., and co-authors. 2003. The common land model. *Bull. Am. Meteorol. Soc.* **84**, 1013–1023.

Dunn, A. L., Barford, C. C., Wofsy, S. C., Goulden, M. L. and Daube, B. C. 2007. A long-term record of carbon exchange in a boreal black spruce forest: means, responses to interannual variability, and decadal trends. *Global Change Biol.* **13**(3), 577–590.

Dutta, K., Schuur, E. A. G., Neff, J. C. and Zimov, S. A. 2006. Potential carbon release from permafrost soils of Northeastern Siberia. *Global Change Biol*. **12**, 2336–2351.

Eliseev, A. V., Arzhanov, M. M., Demchenko, P. F. and Mokhov, I. I. 2009. Changes in climatic characteristics of Northern Hemisphere extratropical land in the 21st century: assessments with the IAP RAS climate model. *Izvestiya Atmos. Ocean Phys.* **45**(3), 271–283.

Euskirchen E. S., McGuire A. D., Kicklighter D. W., Zhuang Q., Clein J. S., and co-authors. 2006. Importance of recent shifts in soil thermal dynamics on growing season length, productivity, and carbon sequestration in terrestrial high-latitude ecosystems. *Global Change Biol*. **12**(4), 731–750.

Farquhar, G. D., von Caemmerer, S. and Berry, J. A. 1980. A biochemical model of photosynthetic CO_2 assimilation in leaves of C3 species. *Planta*. **149**, 78–90.

Fischer, H., Wahlen, M., Smith, J., Mastroianni, D. and Deck, B. 1999. Ice core records of atmospheric CO_2 around the last three glacial terminations. *Science* **283**, 1712–1714.

Frauenfeld, O. W., Zhang, T., Barry, R. G. and Gilichinsky, D. 2004. Interdecadal changes in seasonal freeze and thaw depths in Russia. *J. Geophys. Res.* **109**, doi:10.1029/2003JD004245.

Friedlingstein, P., Cox, P., Betts, R., Bopp, L., Von Bloh, W., and co-authors. 2006. Climate-carbon cycle feedback analysis: results from the (CMIP)-M-4 model intercomparison. *J. Clim.* **19**, 3337–3353.

Indermuhle, A., Stocker, T. F., Joos, F., Fischer, H., Smith, H. J., and co-authors. 1999. Holocene carbon-cycle dynamics based on CO_2 trapped in ice at Taylor Dome, Antarctica. *Nature* **398**, 121–126.

IPCC. 2007. Summary for Policymakers. In: *Climate Change 2007: The Physical Science Basis. Contribution of Working Group I to the Fourth Assessment Report of the Intergovernmental Panel on Climate Change* (eds S. Solomon, D. Qin, M. Manning, Z. Chen, M. Marquis, and co-authors). Cambridge University Press, Cambridge, UK and New York, NY, USA.

Jorgenson, M. T. and Osterkamp, T. E. 2005. Response of boreal ecosystems to varying modes of permafrost degradation. *Can. J. Forest Res.* **35**, 2100–2111.

Khvorostyanov, D. V., Ciais, P., Krinner, G. and Zimov, S. A. 2008. Vulnerability of east Siberia's frozen carbon stores to future warming. *Geophys. Res. Lett.* **35**, doi:10.1029/2008GL033639.

Kicklighter, D. W., Bruno, M., Donges, S., Esser, G., Heimann, M., and co-authors. 1999. A first-order analysis of the potential role of CO_2 fertilization to affect the global carbon budget: a comparison of four terrestrial biosphere models. *Tellus* **51B**, 343–366.

Lawrence, D. M. and Slater, A. G. 2005. A projection of severe near-surface permafrost degradation during the 21st century. *Geophys. Res. Lett.* **32**, doi:10.1029/2005GL025080.

Lawrence, D. M. and Slater, A. G. 2010. The contribution of snow condition trends to future ground climate. *Clim. Dyn.* **34**(7–8), 969–981.

Lawrence, D. M., Slater, A. G., Romanovsky, V. E., Nicolsky, D. J. 2008. Sensitivity of a model projection of near-surface permafrost degradation to soil column depth and representation of soil organic matter. *J. Geophys. Res.* **113**, F02011, doi:10.1029/2007JF000883.

Lemke, P., Ren, J., Alley, R. B., Allison, I., Carrasco, J., and co-authors. 2007. Observations: changes in snow, ice and frozen ground. In: *Climate Change 2007: The Physical Science Basis. Contribution of Working Group I to the Fourth Assessment Report of the Intergovernmental Panel on Climate Change* (eds S. Solomon, D. Qin, M. Manning, Z. Chen, M. Marquis, and co-authors). Cambridge University Press, Cambridge, UK and New York, NY, USA.

Ling, F. and Zhang, T. 2004. A numerical model for surface energy balance and thermal regime of the active layer and permafrost containing unfrozen water. *Cold Regions Sci. Tech.* **38**, 1–15.

Marchenko, S., Romanovsky, V. and Tipenko, G. 2008. Numerical modeling of spatial permafrost dynamics in Alaska. Proceedings, Ninth International Conference on Permafrost. **2**, 1125–1130.

Masarie, K.A. and Tans, P. P. 1995. Extension and integration of atmospheric carbon dioxide data into a globally consistent measurement record. *J. Geophys. Res.* **100**, 11593–11610.

Matthews, E. and Fung, I. 1987. Methane emission from natural wetlands: global distribution, area, and environmental characteristics of sources. *Global Biogeochem. Cycles* **1**, 61–86.

Nakicenovic, N. *et al*. 2000. *Special Report on Emissions Scenarios: A Special Report of Working Group III of the Intergovernmental Panel on Climate Change*. Cambridge University Press, Cambridge, UK, 599.

Nan, Z., Gao, Z., Li, S. and Wu, T. 2003. Permafrost changes in the northern limit of permafrost on the Qinghai-Tibet Plateau in the last 30 years. *Acta Geogr. Sin.* **58**, 817–823.

Oleson, K. W., Dai, Y., Bonan, G., Bosilovich, M., Dickinson, R., and co-authors. 2004. Technical description of the Community Land Model (CLM). NCAR Tech. Note, TN-461+STR, 174 pp.

Osterkamp, T. E. 2007. Characteristics of the recent warming of permafrost in Alaska. *J. Geophys. Res.* **112**, doi:10.1029/2006JF0005788.

Petit, J. R., Jouzel, J., Raynaud, D., Barkov, N. I., Barnola, J. M., and co-authors. 1999. Climate and atmospheric history of the past 420,000 years from the Vostok ice core, Antarctica. *Nature* **399**, 429–436.

Ping, C. L., Michaelson, G. J., Jorgenson, M. T., Kimble, J. M., Epstein, H., and co-authors. 2008. High stocks of soil organic carbon in the North American Arctic region. *Nat. Geosci.* **1**, 615–619.

Qian, H., Joseph, R. and Zeng, N. 2010. Enhanced terrestrial carbon uptake in the Northern High Latitudes in the 21st century from the Coupled Carbon Cycle Climate Model Intercomparison Project model projections. *Global Change Biol.* **16**, 641–656, doi:10.1111/j.1365-2486.2009.01989.x.

Saito, K., Kimoto, M., Zhang, T., Takata, K. and Emori, S. 2007. Evaluating a high-resolution climate model: simulated hydrothermal regimes in frozen ground regions and their change under the global warming scenario. *J. Geophys. Res.* **112**, doi:10.1029/2006JF000577.

Schaefer, K., Collatz, G. J., Tans, P., Denning, A. S., Baker, I., and co-authors. 2008. The combined Simple Biosphere/Carnegie-Ames-Stanford Approach (SiBCASA) Model. *J. Geophys. Res.* **113**, doi:10.1029/2007JG000603.

Schaefer, K., Zhang, T., Slater, A. G., Lu, L., Etringer, A. and Baker, I. 2009. Improving simulated soil temperatures and soil freeze/thaw at high-latitude regions in the Simple Biosphere/Carnegie-Ames-Stanford Approach model. *J. Geophys. Res.* **114**, doi:10.1029/2008JF001125.

Schuur, E. A. G., Bockheim, J., Canadell, J. G., Euskirchen, E., Field, C. B., and co-authors. 2008. Vulnerability of permafrost carbon to climate change. *Implicat. Global Carbon Cycle* **58**(8), 701–714.

Schuur, E. A. G., Vogel, J. G., Crummer, K. G., Lee, H., Sickman, J. O., and co-authors. 2009. The effect of permafrost thaw on old carbon release and net carbon exchange from tundra. *Nature* **459**, doi:10.1038/nature08031.

Sellers, P. J., Tucker, C. J., Collatz, G. J., Los, S. O., Justice, and co-authors. 1994. A global 1° by 1° NDVI data set for climate studies, part II: the generation of global fields of terrestrial biophysical parameters from NDVI. *Int. J. Remote Sens.* **15**, 3519–3545.

Sellers, P. J., Randall, D. A., Collatz, G. J., Berry, J. A., Field, C. B., and co-authors. 1996a. A revised land surface parameterization of GCMs, part I: model formulation. *J. Clim.* **9**, 676–705.

Sellers, P. J., Los, S.O., Tucker, C. J., Justice, C. O., Dazlich, D. A., and co-authors. 1996b. A revised land surface parameterization of GCMs, part II: the generation of global fields of terrestrial biophysical parameters from satellite data. *J. Clim.* **9**, 706–737.

Smith, N. V., Saatchi, S. S. and Randerson, T. 2004. Trends in high latitude soil freeze and thaw cycles from 1988 to 2002. *J. Geophys. Res.* **109**, doi:10.1029/2003JD004472.

Smith, L. C., Sheng, Y., MacDonald, G. M. and Hinzman, L. D. 2005. Disappearing Arctic lakes. *Science* **308**, 1429.

Sushama, L., Laprise, R., Caya, D., Verseghy, D., Allard, M. 2007. An RCM projection of soil thermal and moisture regimes for North American permafrost zones. *Geophys. Res. Lett.* **34**, doi:10.1029/2007GL031385.

Tarnocai, C. 1997. The amount of organic carbon in various soil orders and ecological provinces in Canada. In: *Soil Processes and the Carbon Cycle* (eds R. Lal, J. M. Kimble, R.L.F. Follett and B.A. Stewart). Advances in Soil Science, CRC Press, New York, pp. 81–92.

Tarnocai, C., Canadell, J. G., Schuur, E. A. G., Kuhry, P., Mazhitova, G. and Zimov, S. 2009. Soil organic carbon pools in the northern circumpolar permafrost region. *Global Biogeochem. Cycles* **23**, doi:10.1029/2008GB003327.

Tucker, C. J., Pinzon, J. E., Brown, M. E., Slayback, D. A., Pak, E. W., and co-authors. 2005. An extended AVHRR 8-km NDVI dataset compatible with MODIS and SPOT vegetation NDVI data. *Int. J. Remote Sens.* **26**, 4485–4498.

Uppala, S. M., Kallberg, P. W., Simmons, A. J., Andrae, U., Bechtold, V. D., and co-authors. 2005. The ERA-40 re-analysis. *Q. J. R. Meteorol. Soc.* **131B**, 2961–3012.

Vidale, P. L. and Stockli, R. 2005. Prognostic canopy air space solutions for land surface exchanges. *Theor. Appl. Climatol.* **80**, 245–257.

Walter, K. M., Zimov, S. A., Chanton, J. P., Verbyla, D. and Chapin, F. S. 2006. Methane bubbling from Siberian thaw lakes as a positive feedback to climate warming. *Nature* **443**, 71–75.

Wu, Q. B. and Zhang, T. J. 2008. Recent permafrost warming on the Qinghai-Tibetan plateau. *J. Geophys. Res.* **113**, doi:10.1029/2007JD009539.

Wu, Q. and T. Zhang 2010. Changes in active layer thickness over the Qinghai Tibetan Plateau from 1995 to 2007. *J. Geophys. Res.* **115**, D09107, doi:10.1029/2009JD012974.

Zech, M., Zech, R., Zech, W., Glaser, B., Brodowski, S. and Amelung, W. 2008. Characterisation and palaeoclimate of a loess-like permafrost palaeosol sequence in NE Siberia. *Geoderma* **143**, 281–295.

Zhang, Y., Chen, W. J. and Riseborough, D. W. 2008a. Transient projections of permafrost distribution in Canada during the 21st century under scenarios of climate change. *Global Planet. Change*, **60**(3–4), 443–456.

Zhang, Y., Chen, W. J. and Riseborough, D. W. 2008b. Disequilibrium response of permafrost thaw to climate warming in Canada over 1850–2100. *Geophys. Res. Lett.* **35**, doi:10.1029/2007GL032117.

Zhang, C., Dazlich, D. A., Randall, D.A., Sellers, P. J. and Denning, A. S. 1996. Calculation of the global land surface energy, water, and CO_2 fluxes with an off-line version of SiB_2. *J. Geophys. Res.* **101**, 19061–19075.

Zhang, T., Barry, R. G., Knowles, K., Heginbottom, J. A. and Brown, J. 1999. Statistics and characteristics of permafrost and ground ice distribution in the Northern Hemisphere. *Polar Geogr.* **23**(2), 147–169.

Zhang, T., Frauenfeld, O. W., Serreze, M. C., Etringer, A., Oelke, C., and co-authors. 2005. Spatial and temporal variability in active layer thickness over the Russian Arctic drainage basin. *J. Geophys. Res.* **110**, doi:10.1029/2004JD005642.

Zimov, S. A., Davydov, S. P., Zimova, G. M., Davydova, A. I., Schuur, E. A. G., and co-authors. 2006a. Permafrost carbon: stock and decomposability of a globally significant carbon pool. *Geophys. Res. Lett.* **33**, doi:10.1029/2006GL027484.

Zimov, S. A., Schuur, E. A. G. and Chapin, F. S. 2006b. Permafrost and the global carbon budget. *Science* **312**, 1612–1613.